A Meshless Modeling of Dynamic Strain Localization in Quasi-Brittle Materials Using Radial Basis Function Networks

P. Le[1] N. Mai-Duy[2] T. Tran-Cong[3] and G. Baker[4]

Abstract: This paper describes an integrated radial basis function network (IRBFN) method for the numerical modelling of the dynamics of strain localization due to strain softening in quasi-brittle materials. The IRBFN method is a truly meshless method that is based on an unstructured point collocation procedure. We introduce a new and effective regularization method to enhance the performance of the IRBFN method and alleviate the numerical oscillations associated with weak discontinuity at the elastic wave front. The dynamic response of a one dimensional bar is investigated using both local and non-local continuum models. Numerical results, which compare favourably with those obtained by the FEM and the analytical solutions for a local continuum model, demonstrate the efficiency of the present IRBFN approach in capturing large strain gradients encountered in the present problem.

Keyword: Strain localization, IRBFN, wave propagation, softening materials, quasi-brittle materials.

1 Introduction

In many engineering structures subjected to extreme loading conditions, the initially smooth distribution of strain may change into a highly localised one. Typically, extremely high strains may occur within a very narrow zone while the remaining part of the structure experiences unloading.

Such strain localization usually can be caused by geometrical nonlinearities (e.g., necking of metallic bars) or by material instabilities (e.g., microcracking). Mathematically, the onset of strain localization, in the context of a rate-independent local continuum model, leads to loss of hyperbolicity of the governing partial differential equations, i.e. when the matrix of tangent modulus ceases to be positive-definite. From a computational point of view, the loss of hyperbolicity causes numerical difficulties since the mathematical model becomes ill-posed (localised zone of zero volume). To regularize the ill-posed problems, a number of localization limiters have been developed to ensure that localised zones have a finite volume and the problem becomes well-posed. Examples of localisation limiters include non-local models, rate-dependent models, gradient-dependent models, visco-plastic models, damage-based models, cohesive crack models, smear crack models and Cosserat continuum model.

For one dimensional problems (softening bars), some closed-form exact and approximate solutions have been developed by many authors, including, for example, [Bazant and Belytschko (1985); Sluys (1992); Xin and Chen (2000); Armero and Park (2003)] for the evolution of dynamic strain localization via rate-independent local constitutive models. The above closed-form solutions demonstrated that one of the following two cases is possible. First, if the behavior of the tensile bars is fully elastic, the displacement field is C^0 continuous, the strain field is discontinuous and the discontinuities propagate as incident as well as reflected waves. Second, if localization occurs, the mathematical model becomes ill-posed in the context of a rate-independent local continuum model as stated above. Hence, numerical methods are not able to capture the solutions

[1] CESRC, University of Southern Queensland, Toowoomba, QLD 4350, Australia.
[2] CESRC, University of Southern Queensland, Toowoomba, QLD 4350, Australia.
[3] CESRC, University of Southern Queensland, Toowoomba, QLD 4350, Australia.
[4] DVC(S), University of Southern Queensland, Toowoomba, QLD 4350, Australia.

using rate-independent local constitutive models [Bazant and Belytschko (1985); Sluys (1992); Askes, Bodé, and Sluys (1998)]. Moreover, even if a localization limiter is applied, for an accurate description of the localized zone, a very fine computational mesh is needed, since the strain gradients are very high within localized zones. Hence, robust numerical methods are required to analyze such strain localization phenomena. In general, the position of the localization zone is unknown, therefore, an automatic mesh adaptive procedure is required to increase the efficiency of the numerical method. However, the polynomial approximations in FEM can poorly capture the non-smooth transition between the unloading region with almost constant strain and the localization zone with rapid strain increase [Patzák and Jirásek (2003)] and the FEM results are very sensitive to the computational grids. The extended finite element method [Patzák and Jirásek (2003)], which incorporates special enrichment functions into the shape functions, produces better results, however, the asymptotic solutions are required to be known in advance. Owing the non-local nature of approximations used [Atluri and Zhu (1998); Li and Liu (2000); Batra and Zhang (2004); Atluri and Shen (2002); Han and Atluri (2003, 2004); Le, Mai-Duy, Tran-Cong, and Baker (2007); Wen and Hon (2007)], meshless methods possess some advantages in modelling such strain localization problems and provide more continuous solutions than the piecewise continuous ones obtained from FEM. Thus meshless methods offer effective solutions to the mesh alignment sensitivity in strain localization modelings.

In this study, we report a new numerical method based on radial basis function networks, a truly meshless method, for the analysis of the dynamics of strain localization in 1D problems. The present indirect/integral radial basis function network (IRBFN) method is based on (i) the universal approximation property of RBF networks, (ii) exponential convergence characteristics of the chosen multiquadric (MQ) RBF, (iii) a simple point collocation method of discretisation of the governing equations, and (iv) an indirect/integral (IRBFN)

rather than a direct/differential (DRBFN) approach [Kansa (1990)] for the approximation of functions and derivatives. For the DRBFN, Madych and Nelson (1990) showed that the convergence rate is a decreasing function of derivative order. Since the introduction of the IRBFN approach by [Mai-Duy and Tran-Cong (2001, 2005); Kansa, Power, Fasshauer, and Ling (2004); Ling and Trummer (2004); Mai-Duy, Mai-Cao, and Tran-Cong (2007); Mai-Duy, Khennane, and Tran-Cong (2007)], based on the theoretical result of Madych and Nelson [Madych and Nelson (1990)], concluded that the decreasing rate of convergence can be avoided in the IRBFN approach. Furthermore, the integration constants arisen in the IRBFN approach are helpful in dealing with problems with multiple boundary conditions [Mai-Duy and Tran-Cong (2006)]. However, being a global and high order approximation method, RBF-based methods also suffer from the Gibbs phenomenon where numerical oscillations occur around a jump discontinuity or near a boundary [Jung (2007)], with consequential deterioration of convergence rate, accuracy and stability. In the case of approximation methods based on multiquadric radial basis function (MQ-RBF), several approaches have been developed to attenuate the Gibbs oscillations. For example, Jung (2007) proposed an adaptive piecewise linear basis functions in the vicinity of the discontinuity; Driscoll and Heryudono (2007) suggested an adaptive residual subsampling methods and Le et al [Le, Mai-Duy, Tran-Cong, and Baker (2007)] offered a new coordinate mapping (for boundary-layer problems). In addition, we introduce a new and effective regularization method based on the IRBFN to alleviate numerical oscillations, which enhances the performance of the present method in dealing with weak discontinuities associated with the strain localization process. The paper is organized as follows. The physical problem and its mathematical model are defined in section 2. The numerical formulation for the mathematical model is presented in section 3 which is followed by numerical examples in section 4. Section 5 concludes the paper.

2 Problem definition

Consider a solid bar of of length $2L$, with a unit cross sectional area and mass ρ per unit length as shown in Fig. 1. Let the bar be loaded by forcing both ends to move simultaneously outward, with a constant opposite velocity of magnitude c. The governing equations are described as follows.
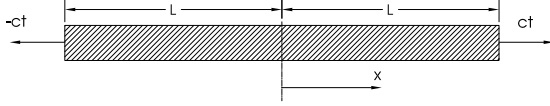
Figure 1: A model of uniform bars.

The momentum equation is given by

$$\rho \frac{\partial^2 u(x,t)}{\partial t^2} = \frac{\partial \sigma(x,t)}{\partial x}, \tag{1}$$

where x is the coordinate measured from the midpoint of the bar, $-L \leq x \leq L$; t is time $0 \leq t \leq t_{max}$; $u(x,t)$ is the displacement in x the direction and $\sigma(x,t)$ is the stress.

The material behaviour is described by a bilinear constitutive law as presented in Fig. 2, which exhibits elastic behavior with Young's modulus E up to strain ε_p at the peak stress f_y (strength), followed by strain-softening (line PF), which has a negative slope E_t up to ε_f, where the stress has a value of zero, finally, followed by a nearly horizontal tail of a very small positive slope E_f.

The constitutive relation is thus given by

$$\triangle \sigma(x,t) = \overline{E} \triangle \varepsilon, \tag{2}$$

in which $\varepsilon = \varepsilon(x,t) = \frac{\partial u(x,t)}{\partial x}$ is the strain and $\overline{E}$ is the slope of the stress-strain relation, defined by

$$\overline{E} = \begin{cases} E, & \text{if } \varepsilon \leq \varepsilon_p, \\ E_t, & \text{if } \varepsilon_p \leq \varepsilon \leq \varepsilon_f, \\ E_f, & \text{if } \varepsilon \geq \varepsilon_f. \end{cases} \tag{3}$$

The boundary conditions are

$$u(x=-L,t) = -ct; \quad u(x=L,t) = ct, \text{ for } t \geq 0. \tag{4}$$
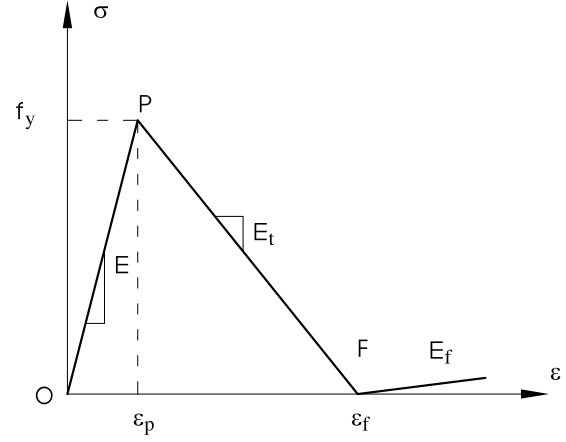
Figure 2: A constitutive relation for quasi-brittle materials.

The initial solutions are taken as follows

$$u(x,t=0)=0 \quad \text{and} \quad \frac{\partial u(x,t=0)}{\partial t} = 0,$$
$$\text{for } -L \leq x \leq L. \tag{5}$$

Due to symmetry, the problem is equivalent to a bar fixed at $x=0$. Thus the boundary conditions for a half model now become

$$u(x=-L,t) = -ct; \quad u(x=0,t)=0, \quad \text{for } t \geq 0. \tag{6}$$

The governing equations are non-dimensionalised using the following scheme: characteristic length a; characteristic time $T = \frac{a}{v_e}$, where $v_e = \sqrt{E/\rho}$ is the elastic wave speed; characteristic stress $\sigma_c = E$; velocities are normalised by v_e, e.g. c/v_e is the dimensionless loading velocity at the ends of the bar. The dimensionless momentum equation is given by

$$\frac{\partial^2 u(x,t)}{\partial t^2} = \left(\frac{ET^2}{\rho a^2} \right) \frac{\partial \sigma(x,t)}{\partial x},$$
$$= \left(\frac{\overline{E}}{E} \right) \gamma^2 \frac{\partial \varepsilon(x,t)}{\partial x}, \tag{7}$$

where $\overline{E}$ is given in Eq. 3, $\gamma = \sqrt{\frac{ET^2}{\rho a^2}} = \frac{v_e T}{a}$.

In the remaining of the paper, for brevity, in addition to (u, x, t, σ), c and L are now dimensionless quantities.

3 Numerical formulation

Consider an initial-boundary-value problem governed by the second order PDE

$$\frac{\partial u}{\partial t} = q_1 \frac{\partial^2 u}{\partial x^2} + q_2 \frac{\partial u}{\partial x} + q_3 u + q_4, \qquad (8)$$

where q_1, q_2, q_3 and q_4 are the coefficients, $0 \leq t \leq T$ and $x_{min} \leq x \leq x_{max}$, with the boundary and initial conditions

$$u(t, x = x_{min}) = u_1, \qquad (9)$$

$$\frac{\partial u}{\partial x}\Big|_{(t, x = x_{max})} = u'_N, \qquad (10)$$

$$u(0, x) = g(x), \qquad (11)$$

in which u_1 and u'_N are given values, and $g(x)$ is a known function.

3.1 Spatial discretisation

In the indirect RBF method (see [Mai-Duy and Tran-Cong (2001, 2005); Mai-Duy (2005); Mai-Duy and Tanner (2005)]), the formulation of the problem starts with the decomposition of the highest order derivative under consideration into RBFs. The derivative expression obtained is then integrated to yield expressions for lower order derivatives and finally for the original function itself. The present work is concerned with the approximation of a function and its derivatives of order up to 2, the formulation can be thus described as follows [Mai-Cao and Tran-Cong (2005); Le, Mai-Duy, Tran-Cong, and Baker (2007)]

$$\frac{d^2 u(x,t)}{dx^2} = \sum_{i=1}^{m} w_i(t) g_i(x) = \sum_{i=1}^{m} w_i(t) H_i^{[2]}(x), \quad (12)$$

$$\begin{aligned}
\frac{du(x,t)}{dx} &= \int \sum_{i=1}^{m} w_i(t) g_i(x) dx + c_1(t) \\
&= \sum_{i=1}^{m} w_i(t) \int g_i(x) dx + c_1(t) \\
&= \sum_{i=1}^{m} w_i(t) H_i^{[1]}(x) + c_1(t), \qquad (13)
\end{aligned}$$

$$\begin{aligned}
u(x,t) &= \sum_{i=1}^{m} w_i(t) \int H_i^{[1]}(x) dx + c_1(t) x + c_2(t) \\
&= \sum_{i=1}^{m} w_i(t) H_i^{[0]}(x) + c_1(t) x + c_2(t), \quad (14)
\end{aligned}$$

where m is the number of RBFs, $\{g_i(x)\}_{i=1}^{m}$ is the set of RBFs, $\{w_i(t)\}_{i=1}^{m}$ is the set of corresponding network weights to be found and $\{H_i^{[j]}(x)\}_{i=1}^{m}$ ($j = 0, 1$) are new basis functions obtained from integrating the radial basis function $g_i(x)$ once or more times. The multiquadrics function is chosen in the present study

$$g_i(x) = \sqrt{(x - c_i)^2 + a_i^2}, \qquad (15)$$

where c_i is the RBF centre and a_i is the RBF width. The width of the ith RBF can be determined according to the following simple relation

$$a_i = \beta d_i, \qquad (16)$$

where β is a factor, $\beta > 0$, and d_i is the distance from the ith centre to its nearest centre. To have the same coefficient vector as Eq. 14, Eq. 12 and Eq. 13 can be rewritten as follows

$$\frac{d^2 u(x,t)}{dx^2} = \sum_{i=1}^{m} w_i(t) H_i^{[2]}(x) + c_1(t).0 + c_2(t).0, \qquad (17)$$

$$\frac{du(x,t)}{dx} = \sum_{i=1}^{m} w_i(t) H_i^{[1]}(x) + c_1(t).1 + c_2(t).0. \qquad (18)$$

Here we choose the RBF centres c_i to be identical to the collocation points x_i, i.e. $\{c_i\}_{i=1}^{m} = \{x_i\}_{i=1}^{N}$. The evaluation of Eq. 17, Eq. 18 and Eq. 14 at a set of N collocation points leads to

$$\begin{aligned}
\mathbf{u}''(t) &= \mathbf{H}^{[2]} \mathbf{w}(t), \qquad (19) \\
\mathbf{u}'(t) &= \mathbf{H}^{[1]} \mathbf{w}(t), \qquad (20) \\
\mathbf{u}(t) &= \mathbf{H}^{[0]} \mathbf{w}(t), \qquad (21)
\end{aligned}$$

where

$$\mathbf{u}''(t) = \left[\frac{\partial^2 u_1(t)}{\partial x^2}, \frac{\partial^2 u_2(t)}{\partial x^2}, \ldots, \frac{\partial^2 u_N(t)}{\partial x^2} \right]^T, \quad (22)$$

$$\mathbf{u}'(t) = \left[\frac{\partial u_1(t)}{\partial x}, \frac{\partial u_2(t)}{\partial x}, \ldots, \frac{\partial u_N(t)}{\partial x} \right]^T, \quad (23)$$

$$\mathbf{u}(t) = [u_1(t), u_2(t), \ldots, u_N(t)]^T, \qquad (24)$$

$$\mathbf{H}^{[2]} =$$

$$\begin{pmatrix} H_1^{[2]}(x_1) & H_2^{[2]}(x_1) & \cdots & H_N^{[2]}(x_1) & 0 & 0 \\ H_1^{[2]}(x_2) & H_2^{[2]}(x_2) & \cdots & H_N^{[2]}(x_2) & 0 & 0 \\ \vdots & \vdots & \ddots & \vdots & \vdots & \vdots \\ H_1^{[2]}(x_N) & H_2^{[2]}(x_N) & \cdots & H_N^{[2]}(x_N) & 0 & 0 \end{pmatrix},$$

$$(25)$$

$$\mathbf{H}^{[1]} =$$

$$\begin{pmatrix} H_1^{[1]}(x_1) & H_2^{[1]}(x_1) & \cdots & H_N^{[1]}(x_1) & 1 & 0 \\ H_1^{[1]}(x_2) & H_2^{[1]}(x_2) & \cdots & H_N^{[1]}(x_2) & 1 & 0 \\ \vdots & \vdots & \ddots & \vdots & \vdots & \vdots \\ H_1^{[1]}(x_N) & H_2^{[1]}(x_N) & \cdots & H_N^{[1]}(x_N) & 1 & 0 \end{pmatrix},$$

$$(26)$$

$$\mathbf{H}^{[0]} =$$

$$\begin{pmatrix} H_1^{[0]}(x_1) & H_2^{[0]}(x_1) & \cdots & H_N^{[0]}(x_1) & x_1 & 1 \\ H_1^{[0]}(x_2) & H_2^{[0]}(x_2) & \cdots & H_N^{[0]}(x_2) & x_2 & 1 \\ \vdots & \vdots & \ddots & \vdots & \vdots & \vdots \\ H_1^{[0]}(x_N) & H_2^{[0]}(x_N) & \cdots & H_N^{[0]}(x_N) & x_N & 1 \end{pmatrix},$$

$$(27)$$

and

$$\mathbf{w}(t) = [w_1(t), ..., w_N(t), c_1(t), c_2(t)]^T. \qquad (28)$$

From an engineering point of view, it would be more convenient to work in the physical space. Owing to the presence of integration constants, the process of converting the networks-weight space into the physical space can also be used to implement Neumann boundary conditions. With the boundary conditions Eq. 9 and Eq. 10, the conversion system can be written as

$$\begin{pmatrix} \mathbf{u}(t) \\ u_N'(t) \end{pmatrix} = \mathbf{C}\mathbf{w}(t), \qquad (29)$$

where $\mathbf{C}$ is the conversion matrix of dimension $(N+1) \times (N+2)$ that comprises the matrix $\mathbf{H}^{[0]}$ and the last row of $\mathbf{H}^{[1]}$. Solving Eq. 29 yields

$$\mathbf{w}(t) = \mathbf{C}^{-1} \begin{pmatrix} \mathbf{u}(t) \\ u_N'(t) \end{pmatrix}. \qquad (30)$$

By substituting Eq. 30 into Eq. 19 and Eq. 20, the values of the second and first derivatives of u with respect to x are thus expressed in terms of nodal variable values and Neumann boundary values

$$\mathbf{u}''(t) = \mathbf{H}^{[2]}\mathbf{C}^{-1} \begin{pmatrix} \mathbf{u}(t) \\ u_N'(t) \end{pmatrix} = \mathbf{D}^{[2]} \begin{pmatrix} \mathbf{u}(t) \\ u_N'(t) \end{pmatrix}, \quad (31)$$

$$\mathbf{u}'(t) = \mathbf{H}^{[1]}\mathbf{C}^{-1} \begin{pmatrix} \mathbf{u}(t) \\ u_N'(t) \end{pmatrix} = \mathbf{D}^{[1]} \begin{pmatrix} \mathbf{u}(t) \\ u_N'(t) \end{pmatrix}. \quad (32)$$

Making use of Eq. 31 and Eq. 32, Eq. 8 can be transformed into the following discrete form

$$\frac{d\mathbf{u}(t)}{dt} = q_1\mathbf{u}''(t) + q_2\mathbf{u}'(t) + q_3\mathbf{u}(t) + \mathbf{q_4}, \qquad (33)$$

or

$$\frac{d\mathbf{u}}{dt} = q_1\mathbf{D}^{[2]} \begin{pmatrix} \mathbf{u}(t) \\ u_N'(t) \end{pmatrix} + q_2\mathbf{D}^{[1]} \begin{pmatrix} \mathbf{u}(t) \\ u_N'(t) \end{pmatrix}$$
$$+ q_3\mathbf{u}(t) + \mathbf{q_4}, \quad (34)$$

where $\mathbf{q_4} = [q_4, q_4, \ldots q_4]^T$ is an $N \times 1$ vector, and

$$\frac{d\mathbf{u}}{dt} = \left[\frac{du_1(t)}{dt}, \frac{du_2(t)}{dt}, \ldots, \frac{du_N(t)}{dt} \right]^T. \qquad (35)$$

Since the values of u_1 and u_N' are given, the unknown vector becomes

$$[u_2(t), u_3(t), \ldots, u_N(t)]^T, \qquad (36)$$

and hence, the first row in Eq. 34 will be removed from the solution procedure. The remainder of Eq. 34 can be integrated in time by using standard solvers such as the Runge-Kutta technique.

3.2 Regularization of IRBFNs and capturing of discontinuous strains

When the displacement field is C^0 continuous (e.g., across a bi-material interface or strain localization); it was found to be difficult to capture accurately the resultant discontinuous strains with conventional FEM. The latter can be improved with the introduction of enriched FEM [Patzák and Jirásek (2003)], however, mesh alignment sensitivity remains a drawback at least for quadrilaterals and embedded discontinuity methods [Li

and Liu (2000)]. On the other hand, several mesh-free methods used special shape functions to account for the jump across a discontinuity [Krongauz and Belytschko (1998); Kim, Liu, Yoon, Belytschko, and Lee (2007)], which seem to work well if the location of discontinuities are known. It will be seen that the present IRBFN method can capture strain discontinuities without suffering any mesh-alignment sensitivities (IRBFN is a truly meshless method) and without having to know the location of discontinuities in advance. However, being a global and high order approximation, the RBFN still produce some oscillations around the discontinuity (Fig. 3). In this study we introduce a new approach where RBFNs can be further regularised to alleviate oscillatory behaviours near such discontinuities.
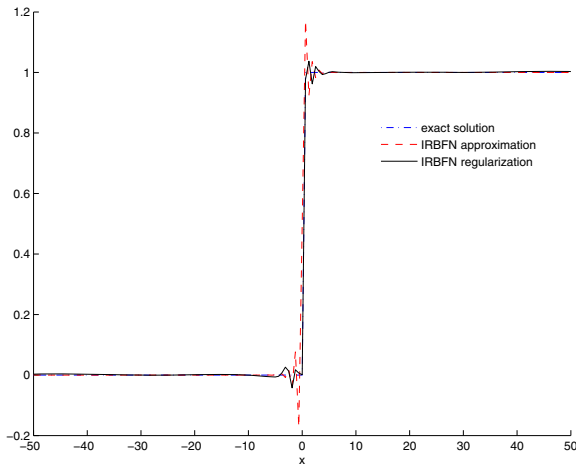
Figure 3: Regularization of IRBFNs.

With noisy data, the generalization performance of RBFNs can be improved using regularization techniques presented in [Orr (1995b)], which are adapted here for IRBFNs. Let $\left\{ (\mathbf{x} = \{x_i\}_{i=1}^N, \hat{\mathbf{y}} = \{\hat{y}_i\}_{i=1}^N) \right\}$ denote the set of input and $f(\mathbf{x})$ the output in the present IRBFN method, the sum-squared-error is

$$S = \sum_{i=1}^N (\hat{y}_i - f(x_i))^2, \tag{37}$$

where N is the number of input data points, $f(x_i)$ is the approximate solution given by Eq. 14 (or

Eq. 21 in matrix form). The output sensitivity to noisy inputs is minimised by augmenting the sum-squared-error with a smoothing term [Orr (1995b)] as follows.

$$C = \sum_{i=1}^N (\hat{y}_i - f(x_i))^2 + \lambda \sum_{j=1}^m w_j^2, \tag{38}$$

where C is a cost function, m is the number of RBF centres, w_j are the network weights, λ is a non-negative regularization parameter. An optimal weight vector $\mathbf{w}$ can be found by minimizing C in Eq. 38 with respect to network weights $\{w_j\}_{j=1}^N$ as follows. Differentiating the cost function C with respect to the network weights $\{w_j\}_{j=1}^N$ yields

$$\frac{\partial C}{\partial w_j} = -2 \sum_{i=1}^N (\hat{y}_i - f(x_i)) \frac{\partial f(x_i)}{\partial w_j} + 2\lambda \sum_{j=1}^m w_j. \tag{39}$$

From Eq. 14 or Eq. 21, $\frac{\partial f(x_i)}{\partial w_j}$ in Eq. 39 can be found simply as

$$\frac{\partial f(x_i)}{\partial w_j} = H_j^{[0]}(x_i), \tag{40}$$

or in compact form

$$\frac{\partial \mathbf{f}}{\partial w_j} = \mathbf{h}_j^{[0]}, \tag{41}$$

where

$$\mathbf{f} = [f(x_1), f(x_2), ..., f(x_N)]^T, \tag{42}$$

and

$$\mathbf{h}_j^{[0]} = \left[H_j^{[0]}(x_1), H_j^{[0]}(x_2), ..., H_j^{[0]}(x_N) \right]^T. \tag{43}$$

Note that vector $\mathbf{h}_j^{[0]}$ is the j-th column of the matrix $\mathbf{H}^{[0]}$ in Eq. 27. Substituting Eq. 41 into Eq. 39 and equating the results to zero lead to

$$\sum_{i=1}^N f(x_i) H_j^{[0]}(x_i) + \lambda w_j = \sum_{i=1}^N y_i H_j^{[0]}(x_i). \tag{44}$$

There are m such equations corresponding to m radial basis functions, $1 \leq j \leq m$, each represents

one constraint on the solution. The resultant system of linear equations like Eq. 44 can be rewritten in matrix form,

$$\left(\mathbf{H}^{[0]}\right)^T \mathbf{f} + \lambda \mathbf{I}_{m+2}\mathbf{w} = \left(\mathbf{H}^{[0]}\right)^T \hat{\mathbf{y}}, \qquad (45)$$

in which $\mathbf{I}_{m+2}$ is an identity matrix of size $(m+2) \times (m+2)$. Solving Eq. 45 leads to the vector of optimal weights

$$\mathbf{w} = \mathbf{A}^{-1} \left(\mathbf{H}^{[0]}\right)^T \hat{\mathbf{y}}, \qquad (46)$$

where

$$\mathbf{A} = \left(\mathbf{H}^{[0]}\right)^T \mathbf{H}^{[0]} + \lambda \mathbf{I}_{m+2}. \qquad (47)$$

Since the performance of the IRBFN regularization completely depends on the regularization parameter λ, an optimal λ must be identified to minimise the error. A number of methods predicting an optimal value of λ automatically have been developed [Orr (1995a,b, 1996)] including the re-estimation method using different error prediction criteria, (e.g. cross-validation, generalized cross-validation, Bayesian information criterion, final prediction error, unbiased estimate of variance). In the present work, the generalized cross-validation (GCV) error prediction criterion is employed as follows.

$$\hat{\sigma}^2 = \frac{N \hat{\mathbf{y}}^T \mathbf{P}^2 \hat{\mathbf{y}}}{[\text{trace}(\mathbf{P})]^2}, \qquad (48)$$

where $\hat{\sigma}^2$ is the variance estimate, N is the number of input data points, $\mathbf{P}$ is the projection matrix, which is defined by

$$\hat{\mathbf{y}} - \mathbf{f} = \hat{\mathbf{y}} - \mathbf{H}^{[0]}\mathbf{A}^{-1}\left(\mathbf{H}^{[0]}\right)^T \hat{\mathbf{y}} = \mathbf{P}\hat{\mathbf{y}}, \qquad (49)$$

in which $\mathbf{P} = \mathbf{I}_N - \mathbf{H}^{[0]}\mathbf{A}^{-1}\left(\mathbf{H}^{[0]}\right)^T$, $\mathbf{I}_N$ is an identity matrix of size $N \times N$. Thus $\mathbf{P}$ relates to the sum-square-error S by

$$S = \hat{\mathbf{y}}^T \mathbf{P}^2 \hat{\mathbf{y}}, \qquad (50)$$

and the cost function C by

$$C = \hat{\mathbf{y}}^T \mathbf{P}\hat{\mathbf{y}}. \qquad (51)$$

Since all the above error prediction criteria relate nonlinearly to λ, a method of nonlinear optimization is required for the estimation of λ. Any standard technique of nonlinear optimization such as the Newton method can be used in this circumstance. Alternately, the optimal value of λ can automatically be determined by a simple iterative procedure [Orr (1996)] as follows.

By differentiating the GCV error prediction and setting the results to zero, a nonlinear equation of λ can be obtained. After some mathematical manipulations, λ can be found iteratively as

$$\lambda = \frac{\hat{\mathbf{y}}^T \mathbf{P}^2 \hat{\mathbf{y}}}{\mathbf{w}^T \mathbf{A}^{-1}\mathbf{w}} \frac{\text{trace}\left(\mathbf{A}^{-1} - \lambda \mathbf{A}^{-2}\right)}{\text{trace}(\mathbf{P})}, \qquad (52)$$

where the right hand side contains λ (explicitly as well as implicitly through $\mathbf{A}^{-1}$ and $\mathbf{P}$). The iterative procedure is started with an initial value of λ for the computation of the right hand side, which is a new estimate of λ, and the process is repeated until convergence.
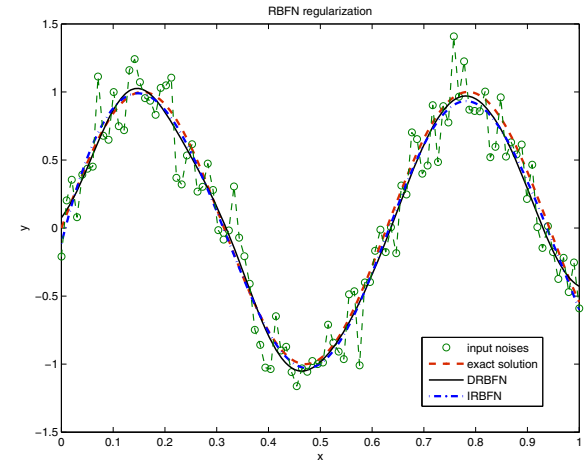
Figure 4: Noisy input, exact solution, DRBFN regularization and IRBFN regularization.

The above regularization method is illustrated with a much improved result as shown in Fig. 3, and further demonstration of the method is given in the following example. Fig. 4 shows the results using 100 noisy input data points and 300 output (test) values obtained by IRBFN and DRBFN regularization methods. The input data are based on

$y = \sin(10x)$, for $0 \leq x \leq 1$, with additional Gaussian noise of standard deviation $\sigma = 0.20$ (the curve with circular marker in Fig. 4). The target (exact) function $y = \sin(10x)$ is depicted by the dash curve. As shown in Fig. 4, the IRBFN regularization method provides a better result (the dot-dash curve) with the mean square error (e_M) of 0.0022 compared with 0.0033 of the DRBFN method (the continuous curve), where e_M is defined as

$$e_M = \frac{\sum_{i=1}^{N}(f(x_i) - y_i)^2}{N}, \tag{53}$$

in which N is the number of test nodes ($N = 300$), $f(x_i)$ the output value and y_i the exact value of the target function. This results is also in good agreement with those of [Mai-Duy (2005)], which showed that the IRBFN method obtained by integration process leads to a better approximation than the DRBFN method by differential process.

4   Numerical examples

For all computations presented in this section, the common dimensionless parameters are chosen as

$$L = 50, \qquad \gamma^2 = \left(\frac{ET^2}{\rho a^2}\right) = 1, \varepsilon_p = 1,$$

$$f_y = 1, \qquad \left(\frac{\overline{E_t}}{E}\right) = -0.70, \qquad \varepsilon_f = 2.4286,$$

$$\left(\frac{\overline{E_f}}{E}\right) = 10^{-6}.$$

Those parameters that are specific to each example are described later where appropriate.

4.1   Wave propagation in fully elastic bars

A uniform bar is loaded by an extensional velocity c of the two ends as shown in Fig. 1. Longitudinal elastic wave propagation precedes strain localisation and is considered in this example. Moreover, if c satisfies the condition $c \leq \varepsilon_p/2$, the behaviour of the bar is purely elastic over the whole computational domain [Bazant and Belytschko (1985)]. The differential equation of motion Eq. 7 reduces to (in dimensionless form)

$$\frac{\partial^2 u(x,t)}{\partial t^2} = \gamma^2 \frac{\partial^2 u(x,t)}{\partial x^2}, \tag{54}$$

which is hyperbolic. The exact solution of Eq. 54 for the given boundary conditions Eq. 4 and the initial solutions Eq. 5 can be found in [Bazant and Belytschko (1985)] and presented for the displacement u and strain ε as follows.

$$u = -c\langle \gamma t - (x+L)\rangle + c\langle \gamma t + (x-L)\rangle,$$
$$0 \leq t \leq \left(\frac{1}{\gamma}\right)2L, \tag{55}$$

where the symbol $\langle\rangle$ is defined by

$$\langle A \rangle = \begin{cases} A, & \text{if } A \geq 0, \\ 0, & \text{if } A < 0, \end{cases} \tag{56}$$

and

$$\varepsilon = \frac{\partial u}{\partial x}$$
$$= c\left[H\left(\gamma t - (x+L)\right)\right] + c\left[H\left(\gamma t + (x-L)\right)\right], \tag{57}$$

in which H denotes the Heaviside step function, defined by

$$H(x) = \begin{cases} 1, & \text{if } x \geq 0, \\ 0, & \text{if } x < 0. \end{cases} \tag{58}$$

The governing equation Eq. 54 involves second-order derivatives of both space and time, and it is convenient to decouple it into a system of first-order equations in both space and time by introducing new variables r and s as follows. Let

$$r = \gamma \frac{\partial u}{\partial x}, \qquad s = \frac{\partial u}{\partial t}, \tag{59}$$

and Eq. 54 is thus equivalent to the system of equations

$$\frac{\partial r}{\partial t} = \gamma \frac{\partial s}{\partial x}, \tag{60}$$

$$\frac{\partial s}{\partial t} = \gamma \frac{\partial r}{\partial x}, \tag{61}$$

subject to the corresponding boundary conditions

$$s(-L,t) = -c, \quad s(L,t) = c, \quad \forall t \in \left[0, \left(\frac{1}{\gamma}\right)2L\right], \tag{62}$$

and the initial solutions

$$r(x,0) = 0, \quad s(x,0) = 0, \quad \forall x \in [-L,L]. \qquad (63)$$

To reduce the computational cost, a half model is analyzed in this section. The equivalent boundary conditions of the half model are

$$s(-L,t) = -c, \quad s(0,t) = 0,$$
$$\forall t \in \left[0, \left(\frac{1}{\gamma}\right) 2L\right], \quad (64)$$

The numerical formulation presented in section 3 is used for solving the system of equations Eq. 60 and Eq. 61 with the boundary conditions Eq. 64 and the initial solutions Eq. 63, with $c = 0.45\varepsilon_p$. The forward Euler formula is used to perform time integration. To satisfy the CFL condition ($\triangle t \leq \frac{1}{\gamma}\triangle x$), the time step is chosen as $\triangle t = 10^{-2}\frac{1}{\gamma}\triangle x$ in this example. The results presented in this example are achieved with 80 uniform collocation points and $\beta = 1$ in Eq. 16. Computations are also carried out with 20, 40, 60 and 100 uniformly distributed collocation points. The obtained solution essentially converges when 40 or more collocation points are used. Fig. 5, Fig. 6 and Fig. 7 show the evolution of the displacement and strain, the numerical results and the exact solutions are plotted on the same graphs. First, the displacement and strain waves propagate from the ends to the center of the bar until these incident waves meet each other at the center at time $t = \left(\frac{1}{\gamma}\right)L$. The zero-th order continuous displacement leads to the strain discontinuity whose position evolves with time as shown in the above figures. As a result of the collision of the two incident waves (at $x = 0$), an abrupt jump of value of strain appears at $x = 0$ (Fig. 8), the strain magnitude is doubled, and the reflection waves propagate outwards to the ends as displayed in Fig. 5(e)-(f)-(g)-(h), Fig. 7 and Fig. 8. The obtained results by the present IRBFN method are in good agreement with the analytical solutions as shown in Fig. 5-Fig. 8.

It is shown that the IRBFN can capture the discontinuous strain in this example, however, there are some oscillations due to the violation of the smoothness assumption inherent in the RBFN approximation. This situation can be improved with regularisation as discussed in section 3.2. When the regularisation parameter λ is set to be equal to 0.07135, it can be seen that the obtained strains shown on the right columns in Fig. 6 and Fig. 7 are much smoother and closer to the exact solutions than those by the standard IRBFN method shown on the left columns of the same figures. Thus, good results are achieved with a general global regularisation of the IRBFNs in contrast with other numerical approaches (discussed in section 3.2) where special treatments must be applied at the elemental level (extended FEM) or special shape functions must be used. Moreover, these special treatments require a priori knowledge of the location of discontinuities while the present IRBFN method does not.

4.2 Wave propagation and strain localization in strain-softening bars: local continuum model

In this example, the problem defined in section 2 is considered with the prescribed velocities at the ends have $c = 0.85\varepsilon_p$, which is above the critical value of $0.5\varepsilon_p$. The behaviour of the bar is elastic until the incident waves meet at the center of the bar (i.e. for $0 \leq t \leq L$) as discussed in section 4.1. Right after the collision of the incident waves, the strain is doubled to $2c = 1.7\varepsilon_p$, causing strain softening and strain localization. From the onset of localization, the computational domain can be divided into two regions with different behaviors: the strain softening and localization zone and the elastic zone. For the elastic domain, the momentum equation Eq. 7 takes the hyperbolic form of Eq. 54 which is solved in the same manner as presented in section 4.1. For the localized zone, the momentum equation becomes elliptic and is solved by a scheme described as follows.

The elliptic momentum equation of the localized zone is

$$\frac{\partial^2 u(x,t)}{\partial t^2} = -\mu^2 \frac{\partial^2 u(x,t)}{\partial x^2}, \qquad (65)$$

in which $\mu^2 = \frac{|E_t|}{E}\frac{ET^2}{\rho a^2}$, and $|E_t|$ is the absolute value of E_t. Eq. 65 can be decoupled into a system
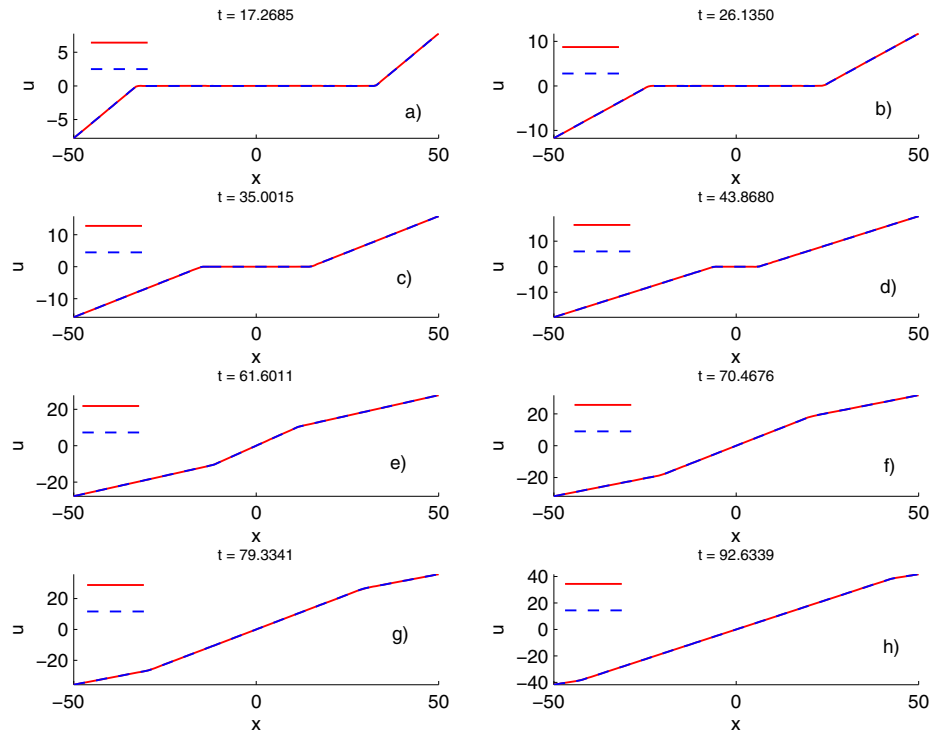
Figure 5: Fully elastic bars: the evolution of displacement, the continuous curves denote the IRBFN solutions and the dash ones the exact solution.
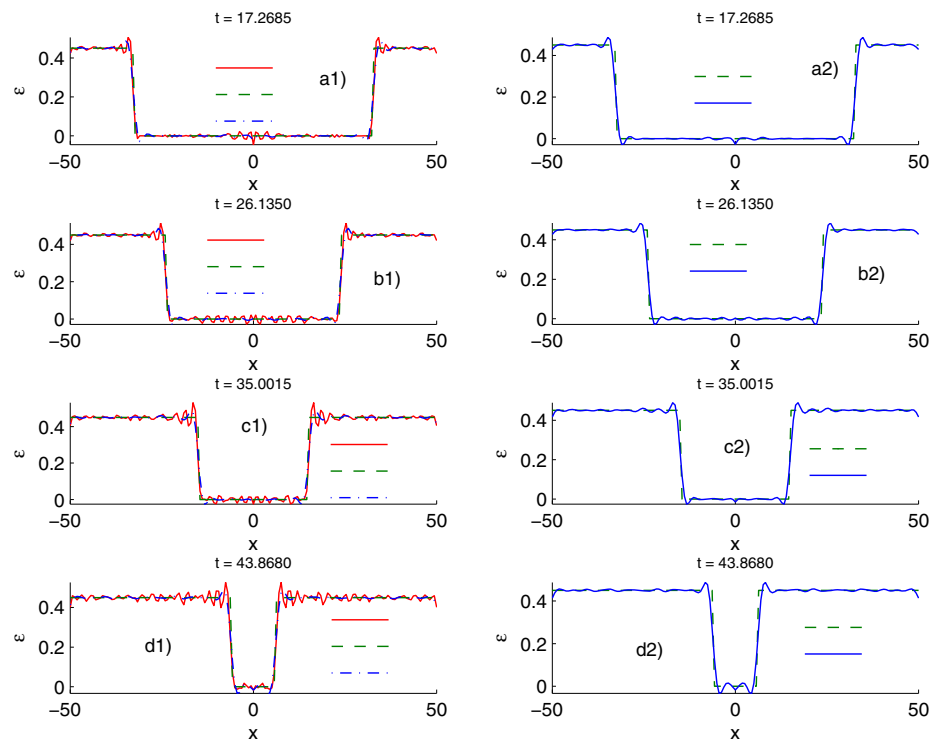
Figure 6: Fully elastic bars: the propagation of step function waves of strain: the continuous curves denote the IRBFN solutions, the dashed ones exact solutions and the dot-dashed curves indicate the IRBFN regularized results on the left column. On the right column, the non-regularized results are removed for clarity.
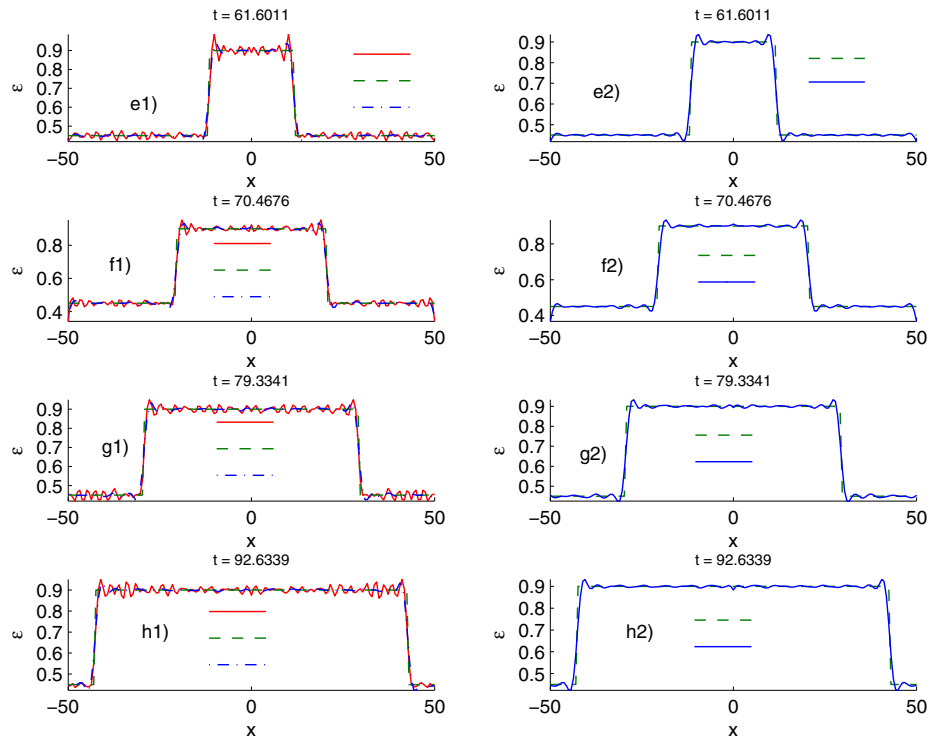
Figure 7: Fully elastic bars: the propagation of step function waves of strain: the continuous curves de-note the IRBFN solutions, the dashed ones exact solutions and the dot-dashed curves indicate the IRBFN regularized results on the left column. On the right column, the non-regularized results are removed for clarity.
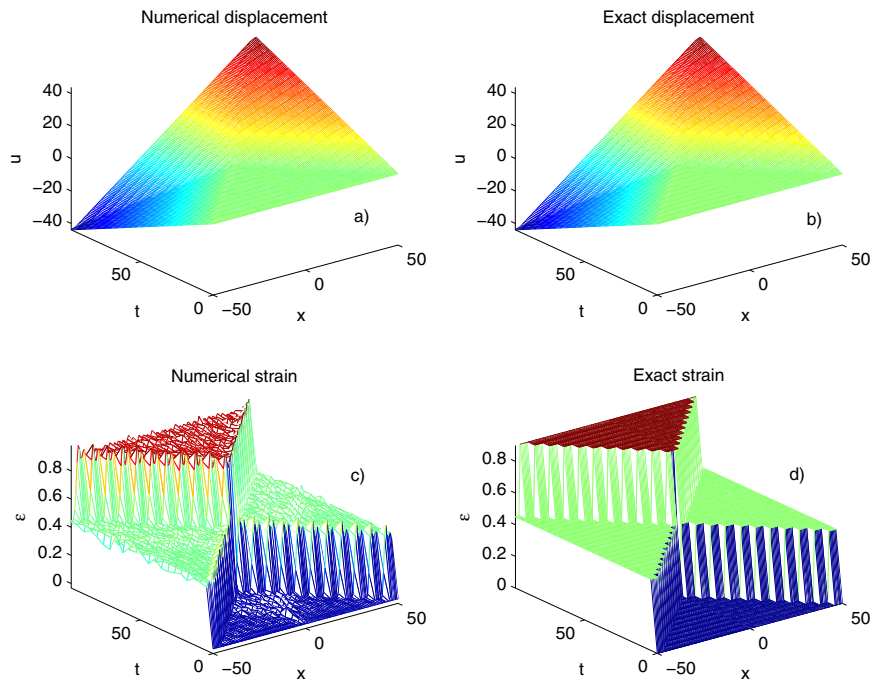
Figure 8: Fully elastic bars: the displacement and strain waves propagations.

of first-order equations in both time and space by letting

$$r = -\mu \frac{\partial u}{\partial x}, \qquad s = \frac{\partial u}{\partial t}, \tag{66}$$

resulting in a system of equations in r and s for the strain-softening zone given by

$$\frac{\partial r}{\partial t} = -\mu \frac{\partial s}{\partial x}, \tag{67}$$

$$\frac{\partial s}{\partial t} = \mu \frac{\partial r}{\partial x}. \tag{68}$$

At the end of the softening process, fracture and rupture will probably occur, however, a fracture criterion is not included in present study, so the material is assumed to be elastic again with a very small elastic modulus $E_f/E = 10^{-6}$. The governing equations in this stage are the same as those in section 4.1, except that the modulus E is replaced by E_f. As before, only a half model needs be discretised (in this case with 80 uniformly distributed nodes). The resultant system of equations is integrated in time by using the forward Euler formula as in section 4.1, where the time step is taken as $\triangle t = 0.25 \times 10^{-4} \frac{\triangle x}{\gamma}$ in this example. The solution of Eq. 67 and Eq. 68 clearly shows the onset of strain localization, characterized by the sudden jump in velocity, displacement, strain and the rapid descent of stress in the localized zone as exhibited in Fig. 9 which depicts the evolution of velocity, displacement, strain and stress at the collocation point $x = -0.6329$, which is the nearest point to the $x = 0$ node. In Fig. 9(d), the stress profile is slightly oscillatory until the loading waves are about to meet. Upon the collision of the incident waves, the stress increases rapidly to the elastic limit f_y then decreases as rapidly down to zero again due to strain-softening. The speedy drop of the stress level is accompanied by the abrupt jump in velocity and rapid increase in displacement and strain as exhibited in Fig. 9(c)-(a)-(b), respectively. Unstable development follows as the localized zone is unable to carry load while the velocity is increasing, the displacement and strain are growing rapidly, two halves of the bar are moving increasingly in two opposite directions like in mode I crack as shown in Fig. 10. In

the next stage of evolution, the velocity and stress increase very slightly while the displacement and strain are growing continuously and quickly because of elastic loading as can be seen in Fig. 9. The steep profiles of stress, velocity and strain are well captured by the present explicit method, although with smaller time steps in comparison with other implicit methods. Fig. 10-Fig.12 depict the spatio-temporal evolution of the displacement, velocity and strain, respectively, while Fig. 13-Fig. 15 show the spatial distribution of velocity, stress, displacement and strain, respectively, at several time instants. The solutions of the elliptic equations yield a standing wave, which is not able to extend outside the localised zone, as illustrated by the strain wave displayed in Fig. 12 and Fig. 15, and the displacement wave in Fig. 10 and Fig. 14 as well. When softening occurs, which is the case here, the localised strain softening zone causes reflection waves travelling backwards from the localised front ($x = 0$), due to sudden unloading.

Fig. 10 and Fig. 14 expose the development of displacement which grows rapidly as a standing wave confined in a very narrow zone. Correspondingly, the increasingly intensive strain within the localized zone is depicted in Fig. 12 and Fig. 15. The velocity is doubled at the onset of localisation and reflected back from the localised zone as shown in Fig. 11 and Fig. 13(a). Similarly, displacement, strain and stress waves also reflected from the localised zone. However, unlike the response in purely elastic bars, the reflected strain wave is out of phase with, and therefore cancelling out the incident strain wave of the same magnitude. Due to the nature of the displacement waves the displacement field in the elastic region is C^0 continuous (Fig. 10 and Fig. 14). The point of C^0 continuous displacement propagates along the elastic region in both directions depending on the stage of loading. Consequently, a discontinuity occurs in the profile of stress, velocity (Fig. 13), and strain (Fig. 15). The oscillatory behaviour of the stress is observed in Fig. 13(b) which was also found in [Sluys (1992); Bazant, Belytschko, and Chang (1984)].

Although the results presented above correspond
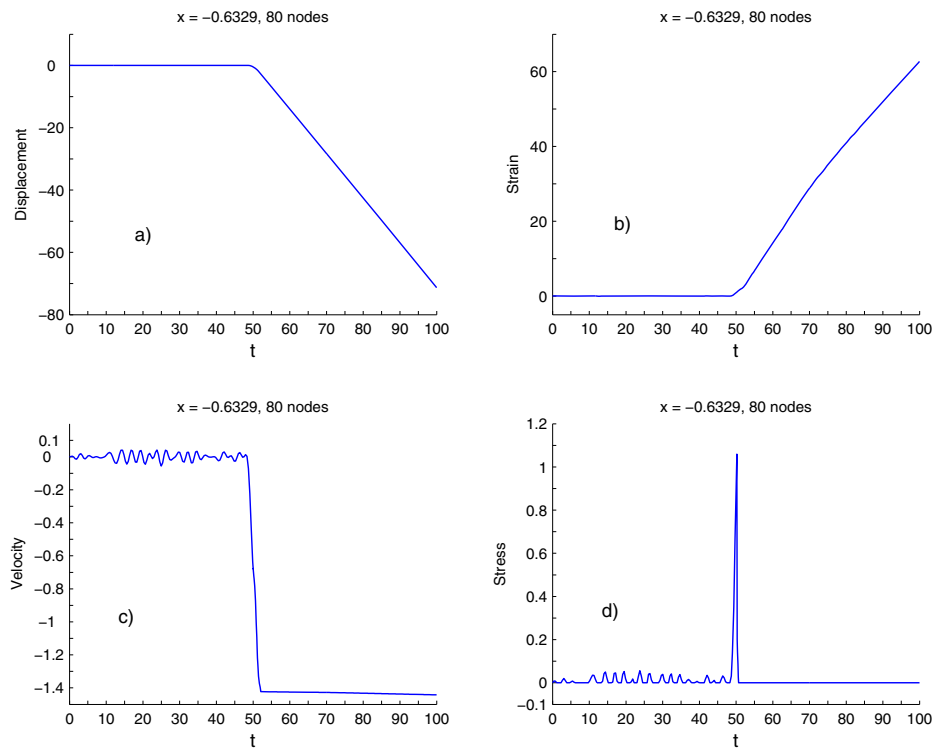
Figure 9: Local continuum model: the evolution of: (a) displacement, (b) strain, (c) velocity and (d) stress at $x = -0.6329$ with 80 uniform collocation points.
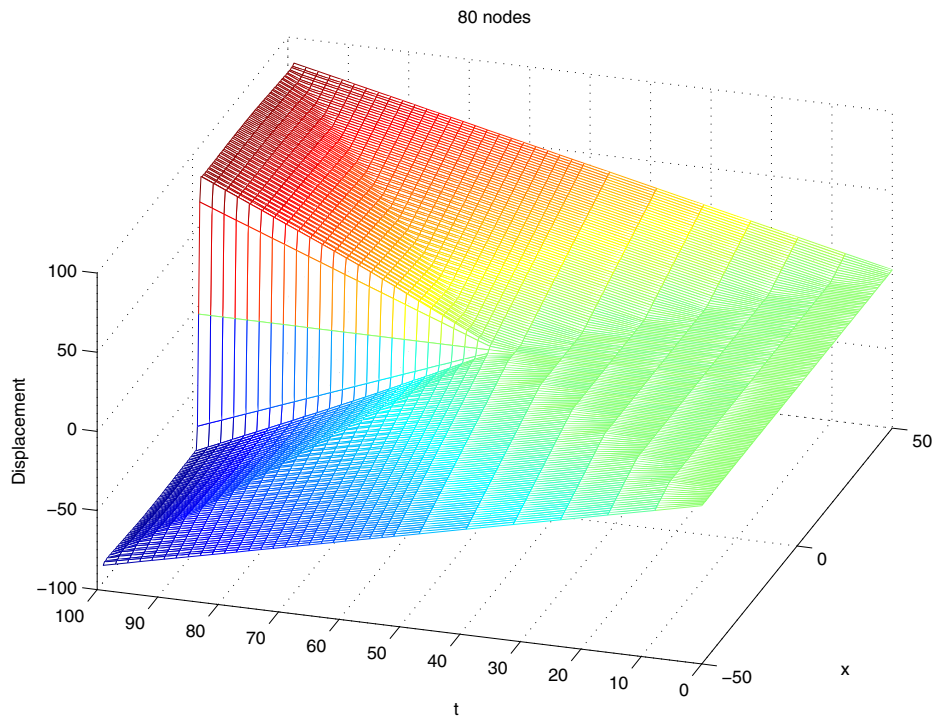
Figure 10: Local continuum model: the evolution of displacement with a uniform discretisation of 80 points.
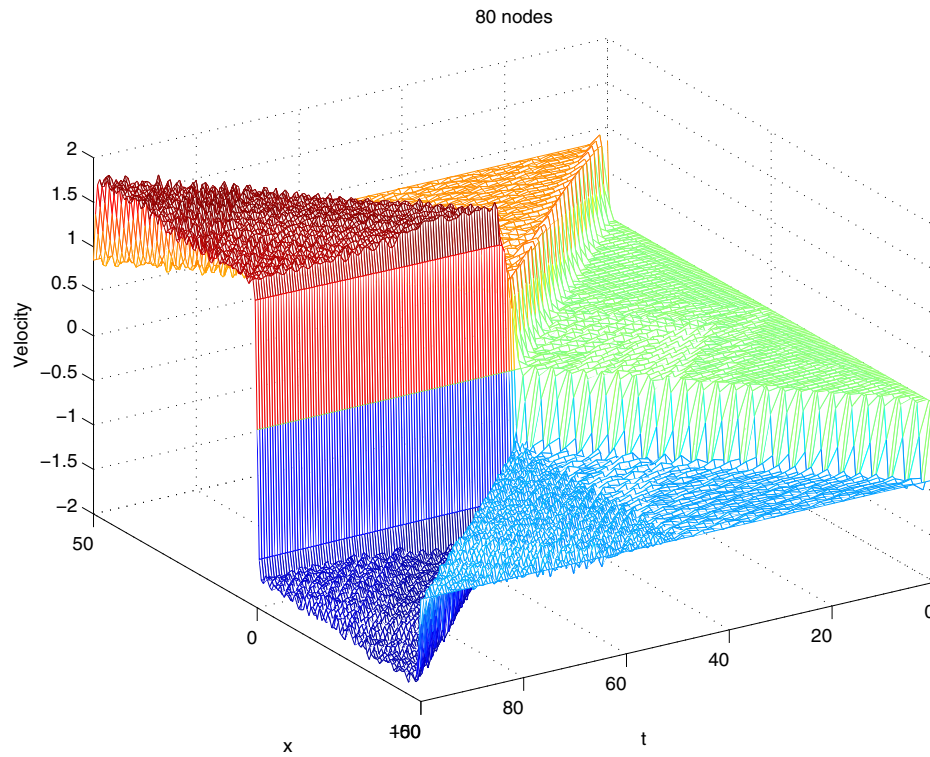
Figure 11: Local continuum model: the evolution of velocity with a uniform discretisation of 80 points.
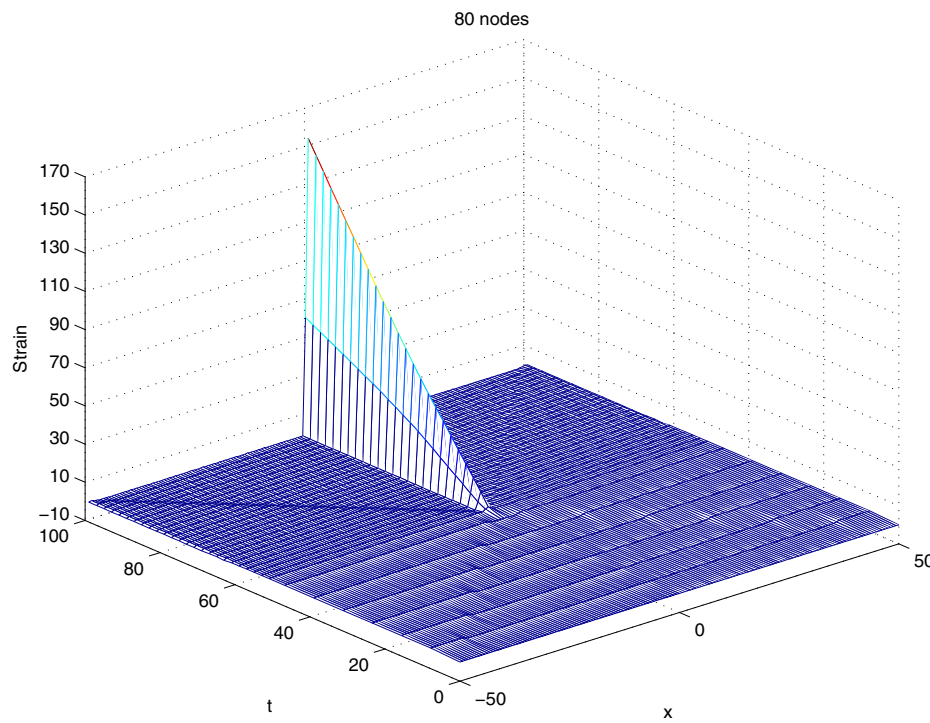
Figure 12: Local continuum model: the evolution of strain with a uniform discretisation of 80 points.
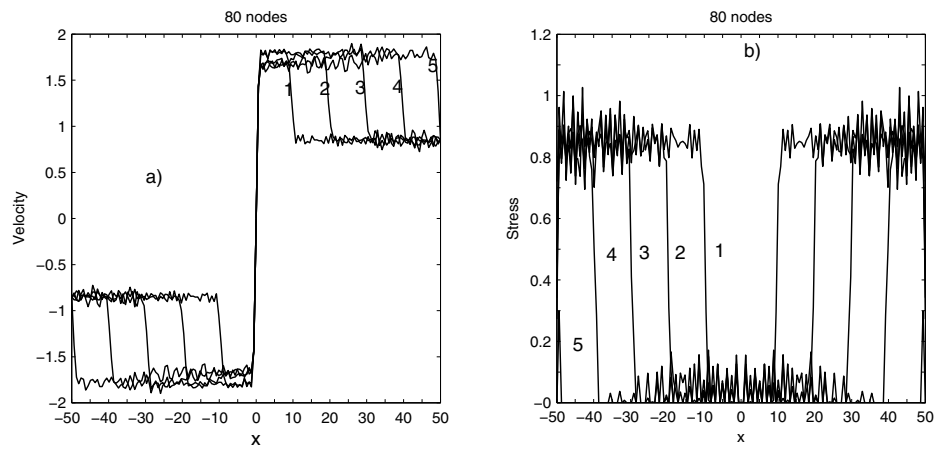
Figure 13: Local continuum model: the curve labels represent time levels: $1(t = 60.0)$; $2(t = 70.0)$; $3(t = 80.0)$; $4(t = 90.0)$; $5(t = 100.0)$ (a) the evolution of velocity, (b) stress obtained with a uniform discretisation of 80 points.
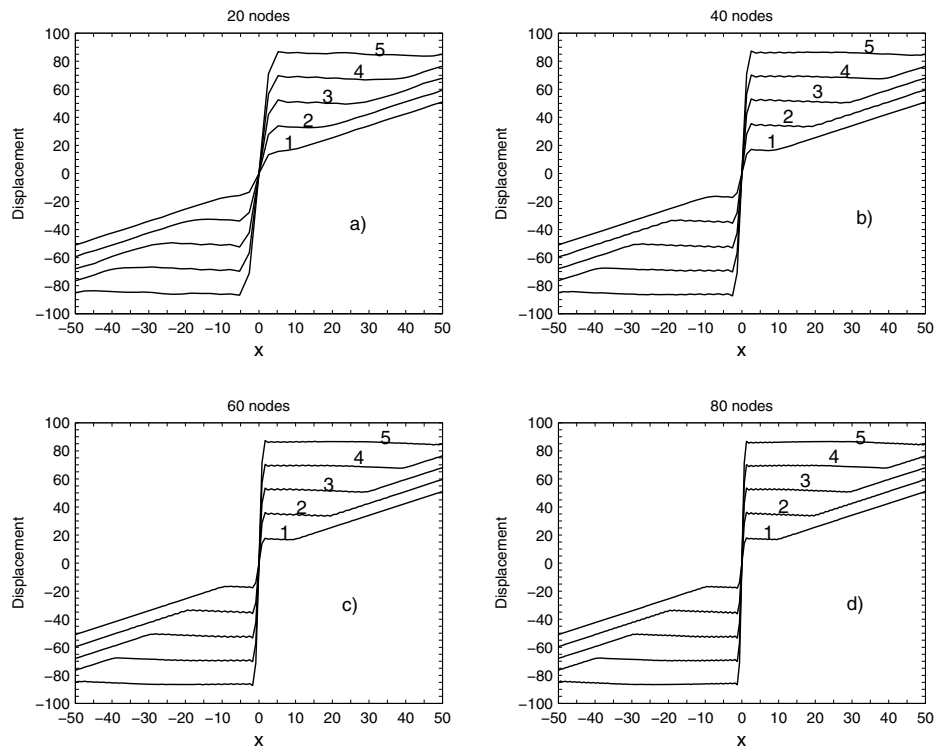
Figure 14: Local continuum model: the evolution of displacement at time levels: $1(t = 60.0)$; $2(t = 70.0)$; $3(t = 80.0)$; $4(t = 90.0)$; $5(t = 100.0)$ (the curve labels indicate time levels) (a) 20 points, (b) 40 points, (c) 60 points and (d) 80 points (uniformly discretised).
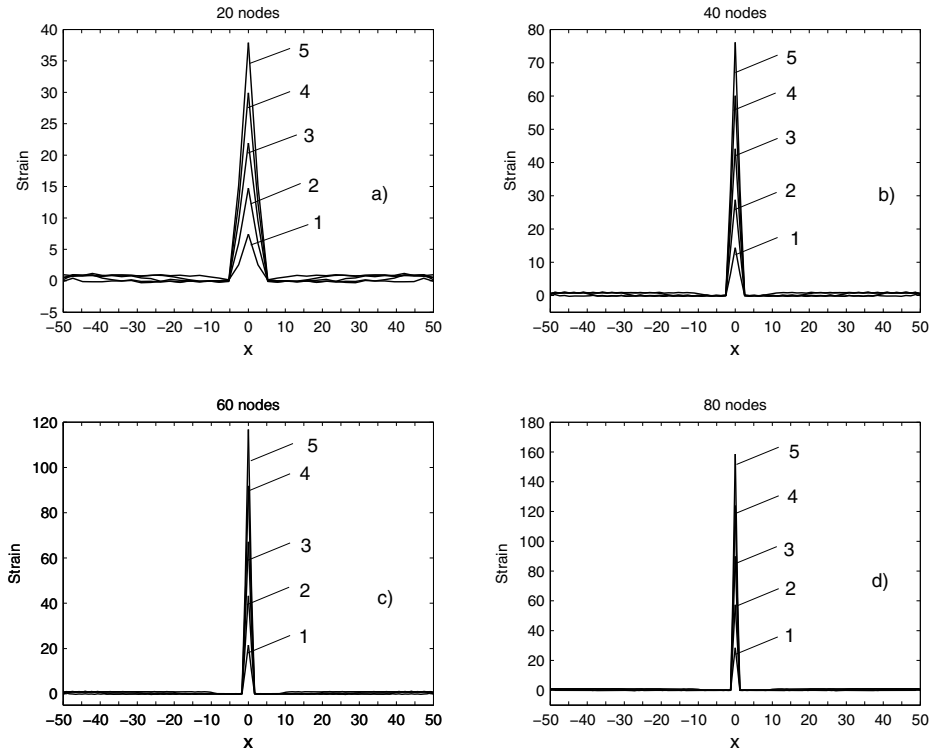
Figure 15: Local continuum model: the evolution of strain at time levels: $1(t = 60.0)$; $2(t = 70.0)$; $3(t = 80.0)$; $4(t = 90.0)$; $5(t = 100.0)$ (a) 20 points, (b) 40 points, (c) 60 points and (d) 80 points (uniformly discretised).

to an 80 point discretisation, computation is also carried out for 20, 40, 60, 100, 120 point discretisations. As the number of collocation points increases, the bandwidth of the localised zone decreases and the maximum strain increases as shown in Fig. 14 and Fig. 15, which is a trend predicted by the exact solution [Bazant and Belytschko (1985)]. However, the zero bandwidth and singular strain associated with the exact model solution cannot be expected to be captured by a numerical method. The obtained results in this section compare favourably with those of the FEM [Sluys (1992); Bazant, Belytschko, and Chang (1984)]. It is worth noting that, unlike the FEM, the present method does not require a priori knowledge of the location of discontinuities which are well captured by a uniform discretisation.

4.3 Wave propagation and strain localization in strain-softening bars: non-local continuum model

In this example, the material is described by a non-local continuum model based on strain averaging or non-local strain. In this model, the local equivalent strain ε is replaced by its non-local counterpart obtained by a weighted average process over a spatial neighbourhood of each point of interest. The non-local strain $\overline{\varepsilon}$ is defined by

$$\overline{\varepsilon}(x,t) = \int_V \alpha(x,\xi)\varepsilon(\xi,t)d\xi, \tag{69}$$

where $\alpha(x,\xi)$ is a given non-local function. In an infinite body, the weight function is assumed to depend only on the distance $r = \| x - \xi \|$ between the "source" point ξ and the "receive" point x. In the vicinity of a boundary, the weight function is usually rescaled such that the non-local operator does not change the uniform field, this means that the weight function satisfies the normalizing con-

dition

$$\int_V \alpha(x, \xi) d\xi = 1, \qquad \forall x \in V. \tag{70}$$

This can be achieved by setting

$$\alpha(x, \xi) = \frac{\alpha_0(\| x - \xi \|)}{\int_V \alpha_0(\| x - \zeta \|) d\zeta}, \tag{71}$$

where $\alpha_0(r)$ is an even and non-negative function of the distance $r = \| x - \xi \|$, monotonically decreasing for $r \geq 0$. It is often taken as the piecewise polynomial bell-shaped function

$$\alpha_0(r) = \begin{cases} \left[1 - \frac{r^2}{R^2} \right]^2, & \text{if } 0 \leq r \leq R, \\ 0, & \text{if } r > R, \end{cases} \tag{72}$$

where R is a parameter related to the internal length of the material. Since R corresponds to the maximum distance of point ξ that affects the non-local average at point x, it is called the *interaction radius* [Patzák and Jirásek (2003)].

The stress-strain relation in Eq. 2 becomes (in dimensionless form)

$$\overline{\sigma}(x, t) = \frac{\overline{E}}{E} \overline{\varepsilon}(x, t), \tag{73}$$

where $\overline{\varepsilon}$ is the non-local strain. Thus the stress in Eq. 73 is also non-local. In order to evaluate $\overline{\varepsilon}$, it is necessary to compute $\varepsilon(\xi, t)$ in Eq. 69, which is accomplished as follows. After an IRBFN discretisation, the vectors of unknown nodal displacements and their corresponding first and second derivatives with respect to x are given by Eq. 21, Eq. 32 and Eq. 31, respectively. Thus, the first order derivative of the displacement with respect to x at an arbitrary point ξ can be written as follows.

$$\frac{\partial u(\xi, t)}{\partial x} = \varepsilon(\xi, t) = H^{[1]}(\xi) \mathbf{C}^{-1} \mathbf{u}(t)$$
$$= D^{[1]}(\xi) \mathbf{u}(t), \quad (74)$$

where $\mathbf{C}^{-1}$ and $\mathbf{u}(t)$ are given by Eq. 30 and Eq. 21, respectively. $H^{[1]}(\xi)$ and $D^{[1]}(\xi)$ are obtained in the same manner that leads to $\mathbf{H}^{[1]}$ and $\mathbf{D}^{[1]}$ in Eq. 32, but with $x = \xi$. Substitution of Eq. 74 into Eq. 69 leads to

$$\overline{\varepsilon}(x, t) = \int_{-R}^{R} \alpha(x, \xi) D^{[1]}(\xi) \mathbf{u}(t) d\xi. \tag{75}$$

Since the nodal variable vector $\mathbf{u}(t)$ is independent of the spatial variable, Eq. 75 can be rewritten as

$$\overline{\varepsilon}(x, t) = \int_{-R}^{R} \alpha(x, \xi) D^{[1]}(\xi) d\xi \mathbf{u}(t) = B(x) \mathbf{u}(t), \tag{76}$$

where

$$B(x) = \int_{-R}^{R} \alpha(x, \xi) D^{[1]}(\xi) d\xi. \tag{77}$$

The momentum equation Eq. 7 becomes

$$\frac{\partial^2 u(x, t)}{\partial t^2} = \left(\frac{\overline{E}}{E} \right) \left(\frac{ET^2}{\rho a^2} \right) \frac{\partial \overline{\sigma}(x, t)}{\partial x}, \tag{78}$$

which, in the elastic case, reduces to

$$\frac{\partial^2 u(x, t)}{\partial t^2} = \gamma^2 \frac{\partial \overline{\varepsilon}(x, t)}{\partial x}. \tag{79}$$

Since the stress and strain are non-local, a new system of governing equations is derived by decoupling the momentum equation Eq. 79 as follows. Let

$$r = \gamma \overline{\varepsilon}(x) = \gamma B(x) \mathbf{u}(t), \qquad s = \frac{\partial u}{\partial t}. \tag{80}$$

After discretisation, the unknown nodal vectors for r and s are, respectively,

$$\mathbf{r}(t) = [r_1(t), r_2(t), \ldots, r_N(t)]^T, \tag{81}$$

and

$$\mathbf{s}(t) = [s_1(t), s_2(t), \ldots, s_N(t)]^T, \tag{82}$$

where N is the number of collocation points. From Eq. 80 and Eq. 82, we have

$$\frac{\partial \mathbf{u}(t)}{\partial t} = \mathbf{s}(t). \tag{83}$$

From Eq. 79, Eq. 80 and Eq. 83, the following system of governing equations, which is equivalent to Eq. 79 (i.e. the elastic case), is obtained

$$\frac{\partial \mathbf{r}(t)}{\partial t} = \gamma \mathbf{B} \mathbf{s}(t), \tag{84}$$

$$\frac{\partial \mathbf{s}(t)}{\partial t} = \gamma \frac{\partial \mathbf{r}}{\partial x}, \qquad (85)$$

where

$$\mathbf{B} = [B(x_1), B(x_2), \dots, B(x_N)]^T, \qquad (86)$$

with $B(x_i) = \int_{-R}^{R} \alpha(x_i, \xi) D^{[1]}(\xi) d\xi, \qquad$ for $i = \overline{1, N}$

and $\frac{\partial \mathbf{r}}{\partial x}$ is obtained by an IRBFN approximation as

$$\frac{\partial \mathbf{r}(t)}{\partial x} = \mathbf{D}^{[1]} \mathbf{r}(t). \qquad (87)$$

For the softening response, the corresponding system of governing equations is

$$\frac{\partial \mathbf{r}(t)}{\partial t} = -\mu \mathbf{B} \mathbf{s}(t), \qquad (88)$$

$$\frac{\partial \mathbf{s}(t)}{\partial t} = \mu \frac{\partial \mathbf{r}}{\partial x}. \qquad (89)$$

The boundary and initial conditions for r and s are the same as those given in section 4.2. As can be seen in the previous two examples, the ramp-like spatial displacement profile results in a discontinuous strain field which can be well captured by the present IRBFN method. However, when a non-local continuum model is used here, the smoothness of the equivalent non-local strain is adversely affected by noises that might exist in the neighbouring strain field. Thus it is found to be advantageous to incorporate IRBFN regularisation into the general IRBFN formulation. The effect of such regularisation is illustrated by considering a ramp function given by

$$\hat{u}(x) = x H(x), \qquad \text{for} \quad -50 \le x \le 50, \qquad (90)$$

where H is the Heaviside function defined in Eq. 58. The exact solution of the first order derivative of $\hat{u}(x)$ with respect to x is

$$\hat{\varepsilon}(x) = \frac{\partial \hat{u}(x)}{\partial x} = H(x). \qquad (91)$$

Let $\tilde{\varepsilon}(x)$ denote the IRBFN approximation of $\frac{\partial \hat{u}(x)}{\partial x}$, which is determined by

$$\tilde{\varepsilon}(x) \approx \frac{\partial \hat{u}(x)}{\partial x} = D^{[1]}(x) \hat{u}(x), \qquad (92)$$

The weighted average of $\tilde{\varepsilon}(x)$, denoted by $\overline{\tilde{\varepsilon}}(x)$, is achieved by replacing $\varepsilon(\xi, t)$ in Eq. 69 by $\tilde{\varepsilon}(x)$

$$\overline{\tilde{\varepsilon}}(x) = \int_V \alpha(x, \xi) \tilde{\varepsilon}(x) d\xi, \qquad (93)$$

The domain is discretised with a uniform distribution of 161 collocation points. The IRBFN parameter $\beta = 1$ in Eq. 16, the interaction radius $R = 5$ in Eq. 93 which is integrated with 11-point Gaussian quadrature, and the IRBFN regularisation parameter is $\lambda = 3.391895$. The results shown in Fig. 16 demonstrate the effectiveness of the present method. In this figure, the exact solution $\hat{\varepsilon}(x)$ is represented by the Heaviside curve; the dot-dashed curve indicates the IRBFN solution $\tilde{\varepsilon}(x)$; the solid curve represents the weighted average of the IRBFN approximation $\overline{\tilde{\varepsilon}}(x)$; the heavy dashed curve represents the regularised weighted average $\overline{\overline{\tilde{\varepsilon}}}(x)$. The above specific parameters, except λ which is dependent on the number of collocation points, are also used in obtaining the results described below.

Returning to the bar problem, the prescribed end velocities are the same as those given in section 4.2, i.e. $c = 0.85\varepsilon_p$. The time step is $10^{-3}\frac{\triangle x}{\gamma}$. Due to the presence of the non-local operator, the full model is analyzed. In fact, in the present computation s is regularised, instead of ε, with similar end results. Fig. 17-Fig. 19 exhibit the evolution of velocity, displacement and non-local strain, respectively. Owing to the properties of non-local weighted average operator, the non-local continuum model yields much smoother response than the corresponding results obtained with a local continuum model, although the evolutionary profiles are similar as expected. The effect of standing wave can be seen in Fig. 18-Fig. 19 (continuous spatio-temporal representation), Fig. 21 and Fig. 22 (at selected times), which show that the growing displacement and strain are confined to the localised zone. The bandwidth of the localized zone and the magnitude of the localized strain are finite, which is in contrast with the the results obtained with a local continuum model, where the exact solution is singular (zero bandwidth localised zone and hence infinite strain). After the onset of strain localization, the velocity, displacement, strain and stress waves reflected from the
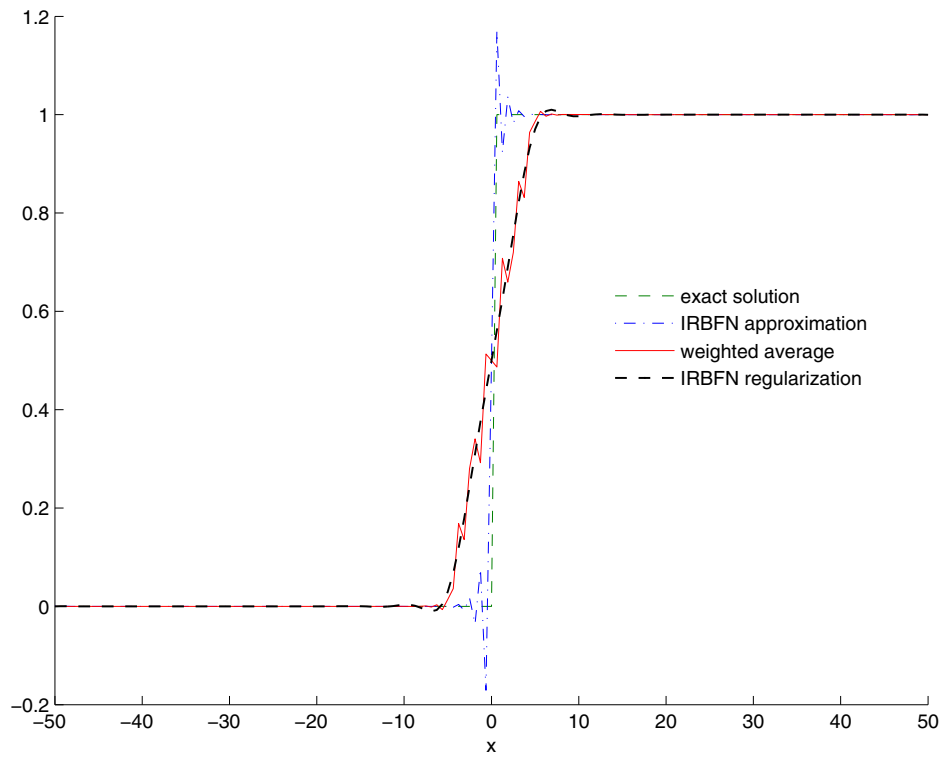
Figure 16: Example of IRBFN regularization.
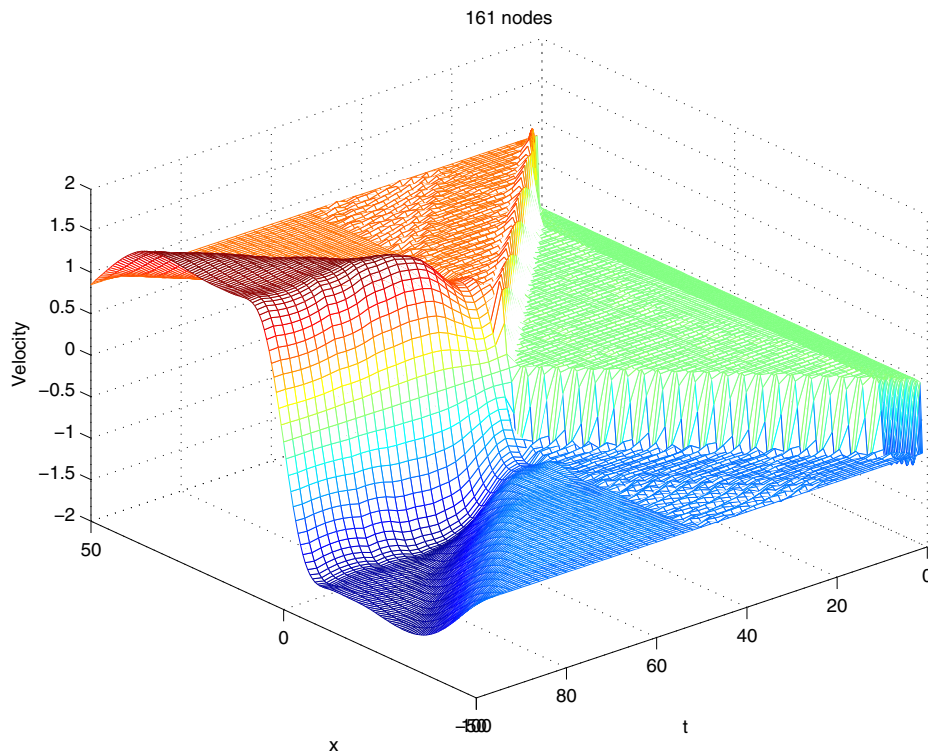
Figure 17: Non-local continuum model: the evolution of velocity with a uniform distribution of 161 collocation points.
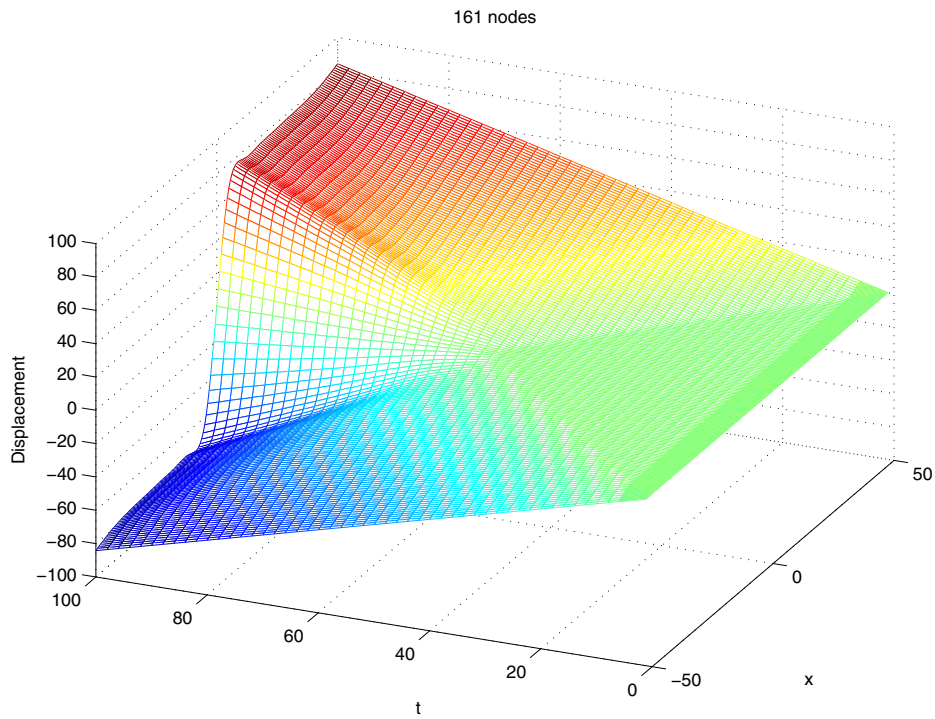
Figure 18: Non-local continuum model: the evolution of displacement with a uniform distribution of 161 collocation points.
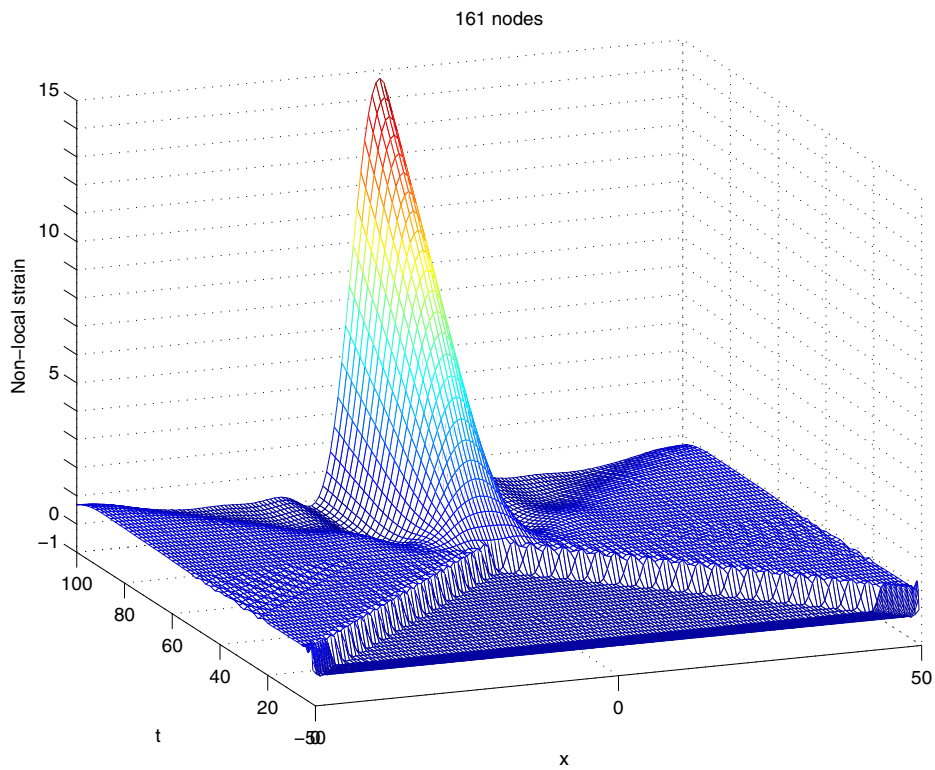
Figure 19: Non-local continuum model: the evolution of non-local strain with a uniform distribution of 161 collocation points.
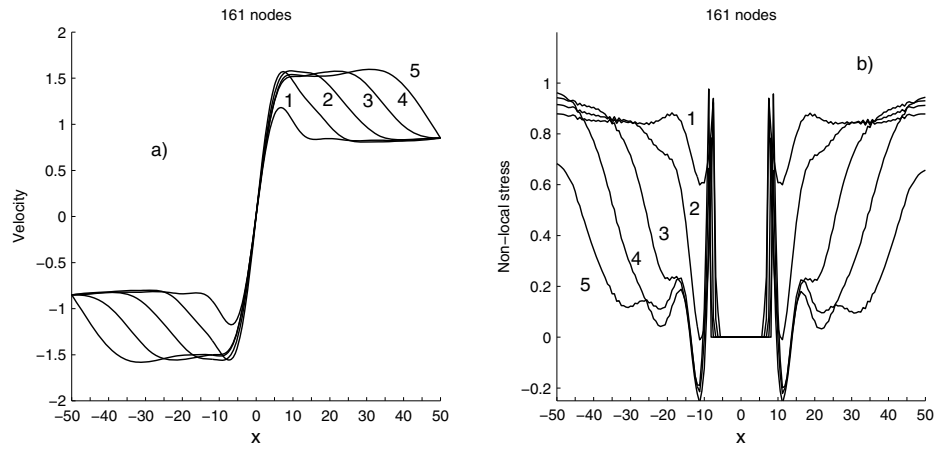
Figure 20: Non-local continuum model: the curve labels represent time levels: $1(t = 60.0)$; $2(t = 70.0)$; $3(t = 80.0)$; $4(t = 90.0)$; $5(t = 100.0)$ (a) the evolution of velocity obtained ,(b) stress obtained with a uniform distribution of 161 collocation points

vskip1em
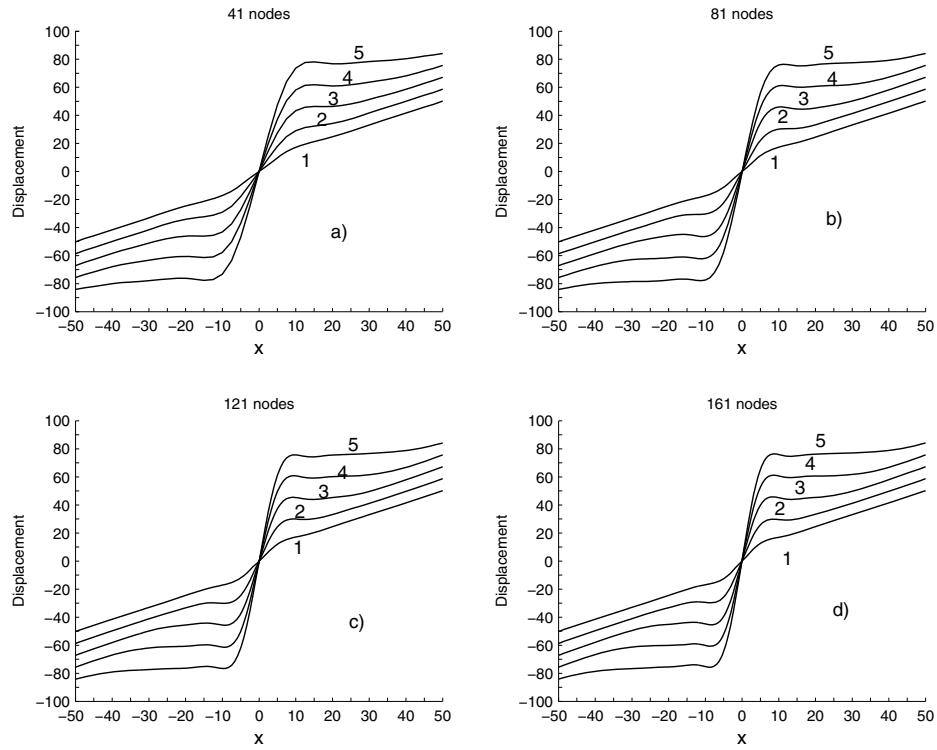
Figure 21: Non-local continuum model: the evolution of displacement at time levels: $1(t = 60.0)$; $2(t = 70.0)$; $3(t = 80.0)$; $4(t = 90.0)$; $5(t = 100.0)$ (the curve labels indicate time levels) (a) 41 points, (b) 81 points, (c) 121 points and (d) 161 points uniformly discretised.

localised zone as shown in Fig. 20-Fig. 22. However, unlike the case of local continuum model, the wave profiles are smooth. In Fig. 20(b), the profiles of stress indicate a complicated loading and unloading process after the initiation of strain localization. There are two narrow zones of high stress at the interfaces between the localized zone and the elastic regions. The standing wave causes the stress to rise in the narrow zones until the elastic limit is reached when sudden unloading occurs due to strain softening effect.

Finally, convergence of the present numerical procedure is demonstrated in Fig. 23 where the non-local strain profiles (at $t = 70.0$) are displayed for a series of collocation points. As discretisation is refined, it can be seen that the bandwidth converges when the number of collocation points is about 160 while the peak non-local strain varies by only 2.3% when the number of collocation points increases from 161 to 241. The slight variation of the peak non-local strain can be expected since the local strain at the centre of the band is singular.

5   Conclusion

An IRBFN meshless method is developed and used to simulate the dynamic strain localization of a bar of quasi-brittle material under dynamic tensile loading. Both local and non-local continuum models are used to describe the material behaviour. The method incorporates a new general and effective regularization method. The enhanced IRBFN approach is able to alleviate the effect of noisy data and capture very well weak discontinuities typical of wave propagation and strain localisation. The present method is able to achieve these results using only uniformly distributed collocation points and requiring no prior knowledge of the location of discontinuities.

References

Armero, F.; Park, J. (2003):   An analysis of strain localization in a shear layer under thermally coupled dynamic conditions. Part 1: Continuum thermoplastic models.   *international journal for numerical methods in engineering*, vol. 56, pp. 2069–2100.

Askes, H.; Bodé, L.; Sluys, L. J. (1998):   ALE nanalyses of localization in wave propagation problems.   *Mechanics of Coheshive-Frictional Materials*, vol. 3, pp. 105–125.

Atluri, S.; Shen, S. (2002):   The meshless local Petrov-Galerkin (MLPG) method:A simple & less-costly alternative to the finite element and the boundary element methods.   *CMES: Computer Modeling in Engineering & Sciences*, vol. 3, pp. 11–51.

Atluri, S. N.; Zhu, T. (1998):   A new meshless local Petrov-Galerkin (MLPG) approach in computational mechanics.   *Comput. Mech.*, vol. 22, pp. 117–127.

Batra, R. C.; Zhang, G. M. (2004):   Analysis of adiabatic shear bands in elasto-thermo-viscoplastic materials by Modified Smooth-Particle Hydrodynamics (SPH) method.   *Journal of Computational Physics*, vol. 201, pp. 172–190.

Bazant, Z. P.; Belytschko, T. (1985):   Wave propagation in a strain softening bar: exact solution.   *journal of Engineering Mechanics (ASCE)*, vol. 111, pp. 381–398.

Bazant, Z. P.; Belytschko, T.; Chang, T. P. (1984):   Continuum theory for strain-softening. *journal of Engineering Mechanics (ASCE)*, vol. 110, pp. 1666–1691.

Driscoll, T. A.; Heryudono, A. R. H. (2007): Adaptive residual subsampling methods for radial basis functions interpolation and collocation problems.   *Computers & Mathematics with Applications*, vol. 53, pp. 927–939.

Han, Z.; Atluri, S. (2004):   A meshless local Petrov-Galerkin (MLPG) approach for 3-diemensional elasto-dynamics.   *CMC: Computers, Materials & Continua*, vol. 1, pp. 129–140.
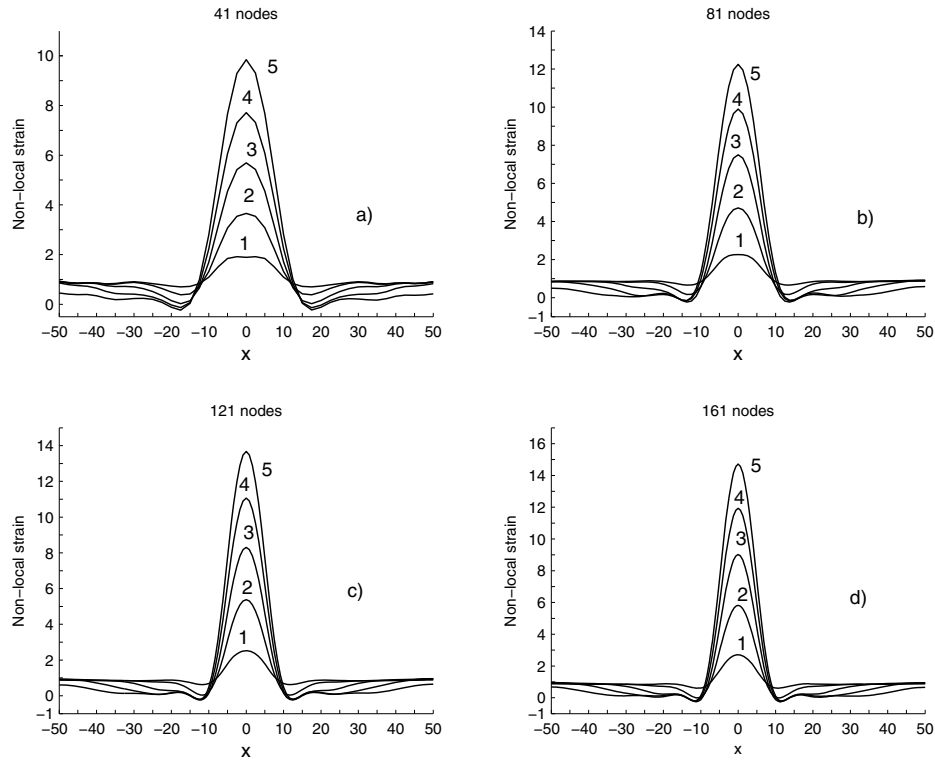
Figure 22: Non-local continuum model: the evolution of non-local strain at time levels: 1($t = 60.0$) ; 2($t = 70.0$) ; 3($t = 80.0$) ; 4($t = 90.0$) ; 5($t = 100.0$) (the curve labels indicate time levels) (a) 41 points, (b) 81 points, (c) 121 points and (d) 161 points uniformly discretised.

vskip1em
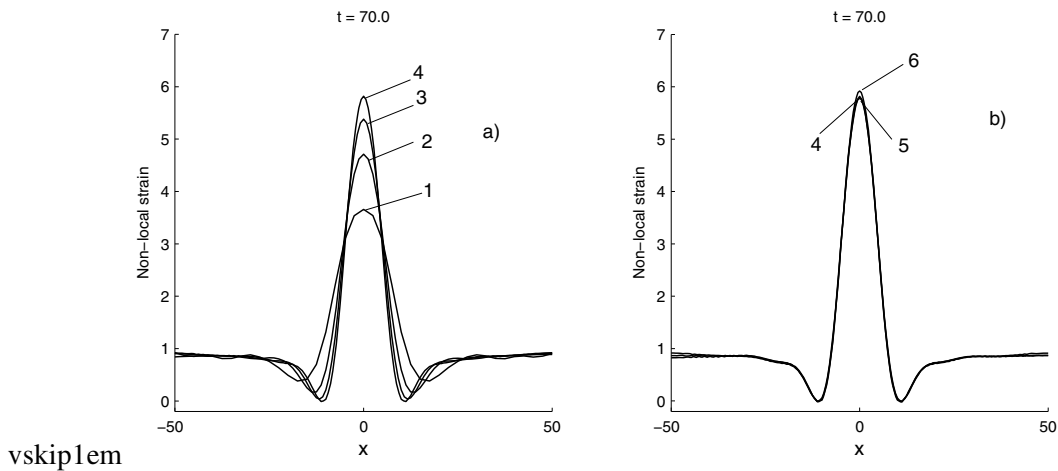
Figure 23: Non-local continuum model: convergence of the solution, the curve labels indicate number of collocation points (CP) as follows. 1(41 CPs, $\lambda = 3.39150$); 2(81 CPs, $\lambda = 3.39150$); 3(121 CPs, $\lambda = 3.39150$); 4(161 CPs, $\lambda = 3.391895$); 5(201 CPs, $\lambda = 6.2267131$); 6(241 CPs, $\lambda = 7.8271318$) at the time $t = 70.0$.

Han, Z. D.; Atluri, S. N. (2003): Truly Meshless Local Petrov-Galerkin (MLPG) Solutions of Traction & Displacement BIEs. *CMES: Computer Modeling in Engineering & Sciences*, vol. 4, no. 6, pp. 665–678.

Jung, J. H. (2007): A note on the Gibbs phenomenon with multiquadratic radial basis functions. *Applied Numerical Mathematics*, vol. 57, pp. 213–229.

Kansa, E. J. (1990): Multiquadrics – a scattered data approximation scheme with applications to computational fluid dynamics – II. Solutions to parabolic, hyperbolic and elliptic partial differential equations. *Computers & Mathematics with Applications*, vol. 19, pp. 147–161.

Kansa, E. J.; Power, H.; Fasshauer, G. E.; Ling, L. (2004): A volumetric integral radial basis function method for time-dependent partial differential equations: I formulation. *Engineering Analysis with Boundary Elements*, vol. 28, pp. 1191–1206.

Kim, D. W.; Liu, W. K.; Yoon, Y.; Belytschko, T.; Lee, S. (2007): Meshfree point collocation method with intrisic enrichment for interface problems (in press). *Computational Mechanics*.

Krongauz, Y.; Belytschko, T. (1998): EFG approximation with discontinuous derivatives. *International Journal for Numerical Methods in Engineering*, vol. 41, pp. 1215–1233.

Le, P.; Mai-Duy, N.; Tran-Cong, T.; Baker, G. (2007): A numerical study of strain localization in elasto-therno-viscoplastic materials using radial basis function networks. *CMC: Computers, Materials & Continua*, vol. 5, pp. 129–150.

Li, S.; Liu, W. C. (2000): Numerical simulation of Strain localization in inelastic solids using mesh-free method. *International Journal for Numerical Methods in Engineering*, vol. 48, pp. 1285–1309.

Ling, L.; Trummer, M. R. (2004): Multiquadratic collocation method with integral formulation for boundary layer problems. *Computers &*

Mathematics with Applications, vol. 48, pp. 927–941.

Madych, W. R.; Nelson, S. A. (1990): Multivariate interpolation and conditionally positive definite functions, II. *Mathematics of Computation*, vol. 54, pp. 211–230.

Mai-Cao, L.; Tran-Cong, T. (2005): A meshless IRBFN-based method for transient problems. *CMES: Computer Modeling in Engineering & Sciences*, vol. 7, pp. 149–171.

Mai-Duy, N. (2005): Solving high order ordinary differential equations with radial basis function networks. *International Journal for Numerical Methods in Engineering*, vol. 62, pp. 824–852.

Mai-Duy, N.; Khennane, A.; Tran-Cong, T. (2007): Computation of laminated composite plates using indirect radial basis function networks. *CMC: Computers, Materials & Continua*, vol. 5, pp. 63–77.

Mai-Duy, N.; Mai-Cao, L.; Tran-Cong, T. (2007): Computation of transient viscous flows using indirect radial basis function networks. *CMES: Computer Modeling in Engineering & Sciences*, vol. 18, pp. 59–77.

Mai-Duy, N.; Tanner, R. I. (2005): Solving high order partial differential equations with indirect radial basis function networks. *International Journal for Numerical Methods in Engineering*, vol. 63, pp. 1636–1654.

Mai-Duy, N.; Tran-Cong, T. (2001): Numerical solution of differential equations using multiquadric radial basic function networks. *Neural Networks*, vol. 14, pp. 185–199.

Mai-Duy, N.; Tran-Cong, T. (2005): An efficient indirect RBFN-based method for numerical solution of PDEs. *Numerical Methods for Partial Differetial Equations*, vol. 21, pp. 770–790.

Mai-Duy, N.; Tran-Cong, T. (2006): Solving biharmonic problems with scattered-point discretization using indirect radial-basis-function networks. *Engineering Analysis with Boundary Elements*, vol. 30, pp. 77–87.

Orr, M. (1995a): Local smoothing of radial basis function networks. In *International Symposium on Artificial Neural Networks*, Hsinchu, Taiwain.

Orr, M. (1995b): Regularisation in the selection of Radial Basis Function Centres. *Neural computation*, vol. 7, pp. 606–623.

Orr, M. (1996):   Introduction to radial basis function networks. *Tecnical report*, Centre for Cognitive Science, University of Edinburgh, Edinburgh EH8 9LW, Scotland, 1996.

Patzák, B.; Jirásek, M. (2003):   Process zone resolution by extended finite elements. *Engineering Fracture Mechanics*, vol. 70, pp. 957–977.

Sluys, L. J. (1992):   *Wave propagation, localisation and dipersion in softening solids*. PhD thesis, Delft University of Technology, 1992.

Wen, P.; Hon, Y. (2007): Geometrically nonlinear alnalysis of Reissner-Mindlin plate by meshless computation. *CMES: Computer Modeling in Engineering & Sciences*, vol. 21, pp. 177–191.

Xin, X.; Chen, Z. (2000): An analytical solution with local elastoplastic models for the evolution of dynamic softenning. *international journal of Solids and Structures*, vol. 37, pp. 5855–5872.